Bioactive Materials 14 (2022) 42–51

Contents lists available at ScienceDirect

Bioactive Materials

journal homepage: www.keaipublishing.com/en/journals/bioactive-materials

Engineering naphthalimide-cyanine integrated near-infrared dye into ROS-responsive nanohybrids for tumor PDT/PTT/chemotherapy

Tongxia Jin [a,c,1], Di Cheng [a,1], Guanyu Jiang [b], Wenqian Xing [a,c], Peiwen Liu [a,c], Bin Wang [a], Weiping Zhu [a,c,*], Haitao Sun [b,***], Zhenrong Sun [b], Yufang Xu [a], Xuhong Qian [a,c,**]

[a] State Key Laboratory of Bioreactor Engineering, Shanghai Key Laboratory of Chemical Biology, School of Pharmacy, East China University of Science and Technology, 130 Meilong Road, Shanghai, 200237, PR China

[b] State Key Laboratory of Precision Spectroscopy, School of Physics and Electronic Science, East China Normal University, 500 Dongchuan Road, Shanghai, 200241, PR China

[c] Shanghai Frontiers Science Center of Optogenetic Techniques for Cell Metabolism, School of Pharmacy, East China University of Science and Technology, 130 Meilong Road, Shanghai, 200237, China

ARTICLE INFO

Keywords:
Near-infrared dye
Integration strategy
Phototherapy
Combination therapy
Drug delivery system

ABSTRACT

Photodynamic (PDT) and photothermal therapies (PTT) are emerging treatments for tumour ablation. Organic dyes such as porphyrin, chlorin, phthalocyanine, boron-dipyrromethene and cyanine are the clinically or pre-clinically used photosensitizer or photothermal agents. Development of structurally diverse near-infrared dyes with long absorption wavelength is of great significance for PDT and PTT. Herein, we report a novel near-infrared dye **ML880** with naphthalimide modified cyanine skeleton. The introduction of naphthalimide moiety results in stronger electron delocalization and larger redshift in emission compared with **IR820**. Furthermore, **ML880** is co-loaded with chemotherapeutic drug into ROS-responsive mesoporous organosilica (**RMON**) to construct nanomedicine **NBD&ML@RMON**, which exhibits remarkable tumor inhibition effects through PDT/PTT/chemotherapy in vivo.

1. Introduction

Near Infrared (NIR) dyes are widely employed in biomedicine, such as fluorescent probes [1], fluorescence-guided surgery [2], photoacoustic imaging [3], phototherapy [4–6], and other fields. Phototherapies, including photodynamic and photothermal therapy, have the advantages of high temporal and spatial accuracy, simple operation and high specificity. Therefore, they are considered as emerging treatments for various tumour ablations. Porphyrin, chlorin, phthalocyanine, boron-dipyrromethene and cyanine derivatives are frequently applied as phototherapeutic agents in preclinical and clinical trials, such as verteporfin [7], bromoaza dipyrromethane ADPM06 [8], indocyanine green (ICG) [9,10]. Nevertheless, the development of structurally diverse near-infrared dyes is of great significance and faces many challenges. The common strategies to construct new NIR dyes include conjugated chain extension, efficient auxochrome utilization, and atom substitution of fluorophore core [11,12]. Yang developed a new class of fluorophores named **ECX** with a five-fused ring, achieving about 300 nm red-shift absorption and emission compared with normal rhodamine [13]. Qian first reported silaanthracene dye, which substituted the oxygen atom with silicon on the rhodamine framework, revealing a 90 nm red-shift [14]. Besides, the covalent connection of traditional dyes is a simple and efficient method to extend wavelength, while retaining the characteristics of traditional dyes. Anthony Romieu's group combined

Peer review under responsibility of KeAi Communications Co., Ltd.

* Corresponding author. State Key Laboratory of Bioreactor Engineering, Shanghai Key Laboratory of Chemical Biology, Shanghai Frontiers Science Center of Optogenetic Techniques for Cell Metabolism, School of Pharmacy, East China University of Science and Technology, 130 Meilong Road, Shanghai, 200237, PR China.

** Corresponding author. State Key Laboratory of Bioreactor Engineering, Shanghai Key Laboratory of Chemical Biology, Shanghai Frontiers Science Center of Optogenetic Techniques for Cell Metabolism, School of Pharmacy, East China University of Science and Technology, 130 Meilong Road, Shanghai, 200237, PR China.

*** Corresponding author. State Key Laboratory of Precision Spectroscopy, School of Physics and Electronic Science, East China Normal University, 500 Dongchuan Road, Shanghai, 200241, PR China.

E-mail addresses: wpzhu@ecust.edu.cn (W. Zhu), htsun@phy.ecnu.edu.cn (H. Sun), xhqian@ecust.edu.cn (X. Qian).

[1] T. Jin and D. Cheng contributed equally to this work.

https://doi.org/10.1016/j.bioactmat.2021.12.009
Received 2 September 2021; Received in revised form 26 November 2021; Accepted 13 December 2021
Available online 20 December 2021

coumarin and hemicyanine to construct a new type of water-soluble NIR fluorophore [15]. Lin integrated rhodamine and merocyanine to get new NIR dyes with long absorption and emission (>700 nm) while retaining the rhodamine-like fluorescence ON-OFF switching mechanisms [16]. The **Flav** [17] and **CX** [18] series dyes, constructed by linking heterocycles with cyanine dyes, exhibited a 200–300 nm redshift than ICG. However, most of them focused on the fluorescence imaging ability, and the photodynamic or photothermal effects of these dyes were not discussed.

Drug delivery systems can provide the platform for the combination of PTT and/or PDT with other traditional treatments to produce additional or even synergistic therapeutic effects [19,20]. Meanwhile the targeting effect of nanohybrids can improve the delivery of phototherapy agents to tumor tissues, making it possible to improve the selectivity and effectiveness of PTT and PDT. Besides, the combination with other therapies may increase the antitumor effect with low-dose photosensitizers or low-power light irradiation, thereby minimizing potential toxicity to healthy tissues. Among the combinational therapy, the combination of PDT/PTT/chemotherapy may provide synergistic therapeutic effects. Chemotherapy can solve the limitation of light penetration in phototherapy, and it may also enhance the sensitivity of cancer cells to hyperthermia or ROS. The phototherapy has a broad spectrum and can solve the problem of chemotherapeutic drug resistance [21–23].

In this work, based on the fluorophore integration strategy, a novel NIR dye **ML880** was designed and synthesized by imitating the cyanine dye polymethine system through a simple synthetic route. The introduction of naphthalimide can result in the enhancement of electron delocalization, and the maximum absorption and emission wavelengths of **ML880** in DMSO were redshifted to 880 nm and 912 nm, respectively, exhibiting remarkable photothermal effects, compared with the commercial dye **IR820**. Furthermore, taking advantage of the high level of reactive oxygen species (ROS) in tumor microenvironment, we constructed a photothermal/ROS dual-responsive degradable drug delivery system **NBD&ML@ RMON** for NIR laser and ROS-assisted combination therapy of hepatocellular carcinoma. The ROS responsive mesoporous organosiloxides (**RMON**) were prepared by H_2O_2-responsive thioacetal fragment organosilane and tetraethoxysilane (TEOS). The NIR dye **ML880**, and a specific inhibitor of Glutathione-S-transferase NBDHEX [24] were co-sealed into **RMON** by using phase change materials (PCM) as the thermal responsive gatekeeper. The **RMON** could be destroyed by intracellular high concentration of H_2O_2 and the ROS produced by **ML880.** Under 880 nm laser irradiation, the photothermal effect of **ML880** melts the PCM, and the loaded cargos will be released, not only realizing PTT/PDT treatment, but also enabling the therapeutic agents' on-demand release at tumor sites (Scheme 1).

2. Materials and methods

2.1. Materials and apparatus

Unless otherwise stated, all reagents were purchased from commercial suppliers and used without further purification. ^{1}H NMR and ^{13}C NMR spectra were measured on a Bruker AMX-400 NMR spectrometer and Bruker Ascend 600 NMR spectrometer, using TMS as an internal standard. High resolution mass spectrometric (HRMS) analyses were carried out in a HP 1100 LC-MS spectrometer. UV–visible spectra and fluorescence spectra were measured on a Horiba Duetta. Deionized water was purified using a Millipore Milli-Q A10 super-water system. The size distribution and zeta potential of nanohybrid were measured by dynamic light scattering (DLS) detector (Zetasizer Nano-ZS90, Malvern Instruments Ltd, UK). The morphology of nanoparticles was photographed by high resolution transmission electron microscope (JEM-2100, Japan) and field emission scanning electron microscope (S-4800, Japan). Pore size distribution and pore volume were obtained by the Surface Area and Porosimetry System (ASAP2010 N, USA). Fluorescence images were collected on an A1R confocal laser scanning microscope (CLSM, Nikon, Japan).

2.2. Preparation of ML880

ML880 was synthesized through a five-step route (Scheme 1A). The commercial compound 4-bromo-1,8-naphthalene anhydride was first substituted by n-butylamine, obtaining compound **ML-1** [25–27]. **ML-1** was then reacted with hydrazine hydrate to obtain compound **ML-2** [28], followed by Fischer indole synthesis to obtain compound **ML-3** [29]. Ammonium salt formation was performed by using **ML-3** with 1, 3-propanesultone to afford **ML-4** [30–32]. The positive charge of

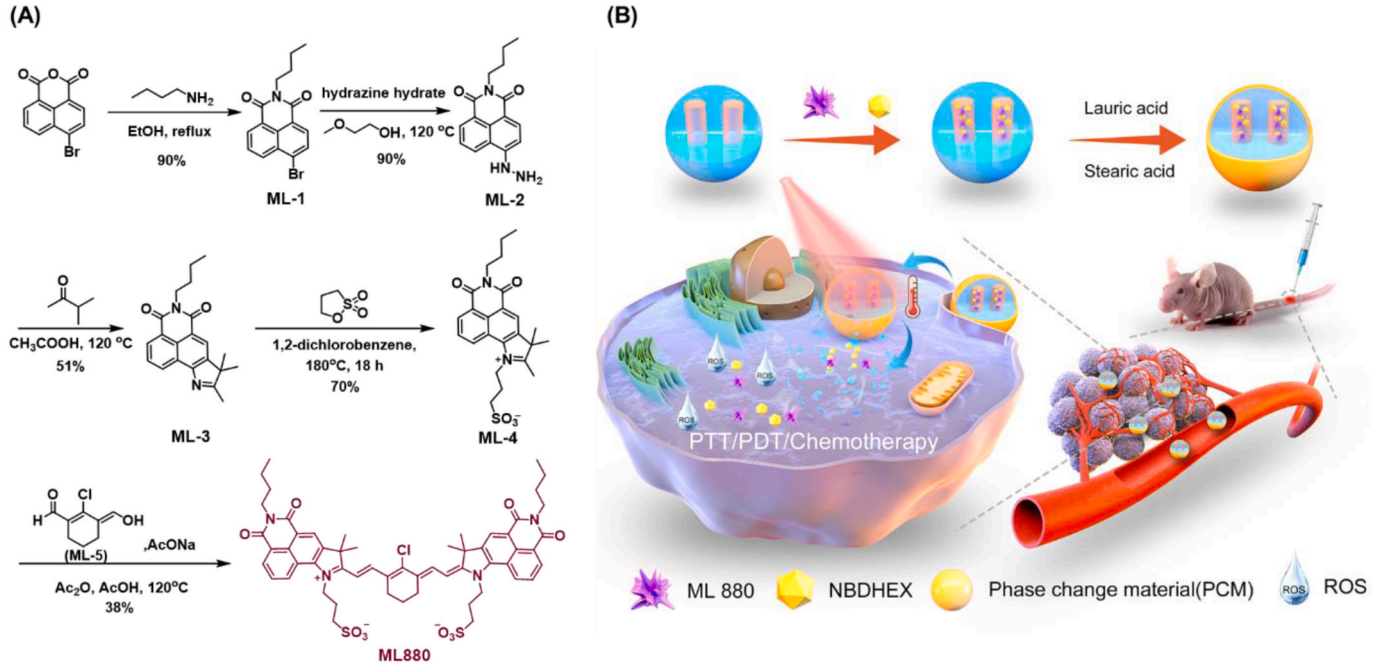

Scheme 1. (A) The synthesis route of NIR fluorophore **ML880**; (B) The schematic illustration of the preparation and function of nanohybrids.

pyrrolidinium ion of **ML-4** makes the α-methyl group acidic thus enabling it to condense on both sides with the aldehydic and vinylic alcohol of **ML-5** to yield the desired product **ML880** [33–35]. The structure of **ML880** was confirmed by ^{1}H NMR and ^{13}C NMR spectral and ESI-MS. The detailed operational processes were supplied in Supporting Information.

2.3. Preparation of NBD&ML@RMON

NBDHEX (15 mg), **ML880** (10 mg), and **RMON** (50 mg) were dissolved in deionized water (10% DMSO, v/v), and the mixture was stirred in room temperature for 48 h at Ar circumstance in the dark. Precipitate was obtained by repeated centrifugation (8000 rpm, 5 min) until the supernate became colorless, and the solid was then freeze-dried. The solid was added to the DMSO solution (0.2 mL, lauric acid: 40 mg, stearic acid: 10 mg), and centrifuged at 10000 rpm for 3 min after shaking for 5 min. The sediments were washed twice with DMSO, and then 0.6 mL of deionized water was added to solidify the fatty acids and freeze dry the **NBD&ML@RMON**.

2.4. Photothermal performance

The photothermal performance of **ML880** and **NBD&ML@RMON** under 880 nm laser irradiation was examined in PBS solution (pH = 7.4) in quartz cuvettes. Temperature changes were recorded longitudinally by employing a sensitive thermosensor.

2.5. Photodynamic performance

1,3-diphenylisobenzofuran (DPBF), an $^{1}O_2$ detection reagent, was used to detect extracellular singlet oxygen. 2′,7′-Dichlorodihydrofluorescein diacetate (DCFH-DA) was used to detect cellular ROS. Cells provided by Shanghai Meixuan Biological science and technology LTD were cultured in DMEM containing 10% FBS and 1% penicillin-streptomycin (100 units mL^{-1} of both) at 37 °C under a humidified atmosphere with 5% CO_2.

HepG2 cells were incubated in confocal dishes for 24 h. After replacing the original medium, the HepG2 cells were incubated with a fresh medium containing **ML880** or **NBD&ML@RMON**. Then the cells were incubated with a serum-free medium containing 1 μg mL^{-1} of Hoechst for 10 min and 10 μM of DCFH-DA for 30 min. After replacing the medium with a fresh medium, dishes were illuminated with or without 880 nm laser. Images were captured using CLSM.

2.6. Cell viability

MTT reagent was used for cell viability analysis. The cells with a good growth state and in the logarithmic growth period were first seeded into 96-well cell culture plates. Each group has 6 multiple wells, and the inoculation density was 7 × 10^3/well. Then the culture plates were put into a cell incubator (37 °C, 5% CO_2). After cells were adhered to the bottom of each well, the complete medium of each well was discarded and washed twice with fresh DMEM. Subsequently, HepG2 cells were immersed in 100 μL of complete medium containing **ML880** or nanohybrids at various concentrations for 24 h. Each well was illuminated with or without an 880 nm laser for 5 min respectively after replacement of the old medium. Then the mixed MTT solution (5 mg mL^{-1}, 20 μL) was added to each well. The old medium was replaced with 200 μL of DMSO after 4 h to dissolve the formazan crystals that exist in the mitochondria of living cells. The percentage of cells which were viable was calculated by measuring the absorbance intensity at 492 nm and 630 nm using a microplate reader.

2.7. Animal experiments

Female BALB/c nude mice were purchased from Shanghai SLAC Laboratory Animal Co., Ltd. and used under protocols approved by the Scientific Investigation Board of the East China University of Science and Technology. The volume of tumors was calculated as: Volume = (a × b^2)/2, where a represents the longest diameter and b represents the shortest diameter. Six-week-old female BALB/c nude mice with around 100 mm^3 HepG2 tumor xenografts were randomly divided into seven groups (n = 5 each). Each group of mice received a different treatment, as follows. Group 1: 100 μL saline; Group 2: 100 μL free NBDHEX (1.5 mg kg^{-1}); Group 3: 100 μL **NBD@RMON** (20 mg kg^{-1}); Group 4: 100 μL **ML@RMON** (20 mg kg^{-1}); Group 5: 100 μL **ML@RMON** (20 mg kg^{-1}), NIR laser irradiated for 5 min; Group 6: 100 μL **NBD&ML@RMON** (30 mg kg^{-1}); and Group 7: 100 μL **NBD&ML@RMON** (30 mg kg^{-1}), NIR laser irradiated for 5 min. The treatment period was 15 days. Each group was injected every three days, and the body weight and tumor sizes were recorded every three days. Groups 5 and 7 were irradiated 18 h after intravenous injection.

3. Results and discussion

3.1. Optical properties of ML880

The absorption and emission features of **ML880** were explored in various solvents as shown in Table 1 and Fig. S1. As expected, the maximum absorption and emission wavelengths of the **ML880** fall in the near-infrared region of 850–940 nm, indicating that the integration strategy to construct new NIR dye based on traditional dye naphthalimide and cyanine was successful. In DMSO, the maximum absorption and emission wavelength of **ML880** was 880 nm and 912 nm, respectively. Taking the reported dye **ECX** [13] as the reference, the fluorescence quantum yield of **ML880** in DMSO was 0.11, and the extinction coefficient reached 8.84 × 10^4 (Table 1). Furthermore, the pH tradition showed that **ML880** stayed stable in the range of pH 4–8 (Fig. S2).

To explain the spectral redshift mechanism of **ML880**, density functional theory (DFT) and time-dependent DFT (TDDFT) calculations were further performed to study the corresponding optimized geometry and electronic structure compared to **IR820** as a reference (see Fig. 1). As shown in Table S1, the bond lengths of bonds A-H were listed and the molecular skeleton displayed a symmetrical structure with similar bond lengths for bonds A-D and bonds E-H. The bond lengths of bond A/C in **ML880** (1.3929 Å/1.4062 Å) were longer than those of **IR820** (1.3916 Å/1.4054 Å). Oppositely, bond B/D in **ML880** (1.4046 Å/1.4172 Å) was shorter than those in **IR820** (1.4086 Å/1.4178 Å). Compared to **IR820**, the long bond in **ML880** became shorter and short bonds became longer, indicating that **ML880** possessed a more delocalized electronic structure. According to the TDDFT results as shown in Table S2, the calculated emission wavelengths at the optimally-tuned TD-PCM(DMSO)-LC-BLYP*/6-311G(d) level well reproduced the experimental measurements, suggesting the reliability of the current level of the method. Moreover, the lowest singlet excited state (S_1) of **ML880** and **IR820** consisted of a pure LUMO → HOMO transition with significant localized excitation character along the whole molecular backbone.

To further study the fragment's contributions to HOMO/LUMO orbitals (Table S3), **ML880** and **IR820** were divided into three fragments (fragment 1 & 3 and fragment 2) as shown in Fig. 1A and D.

Table 1
Photophysical characterization of **ML880** in different solvents.

ML880	$\lambda_{max,abs}$ [nm]	$\lambda_{max,em}$ [nm]	ε [M^{-1} cm^{-1}]	Φ_F (%)
PBS	936	*NA*	58000	*NA*
DMSO	880	912	88390	11.1
MeCN	862	886	36350	13.8
DMF	868	901	18600	13.1
MeOH	856	884	45890	8.2
EtOH	862	892	41720	10.1

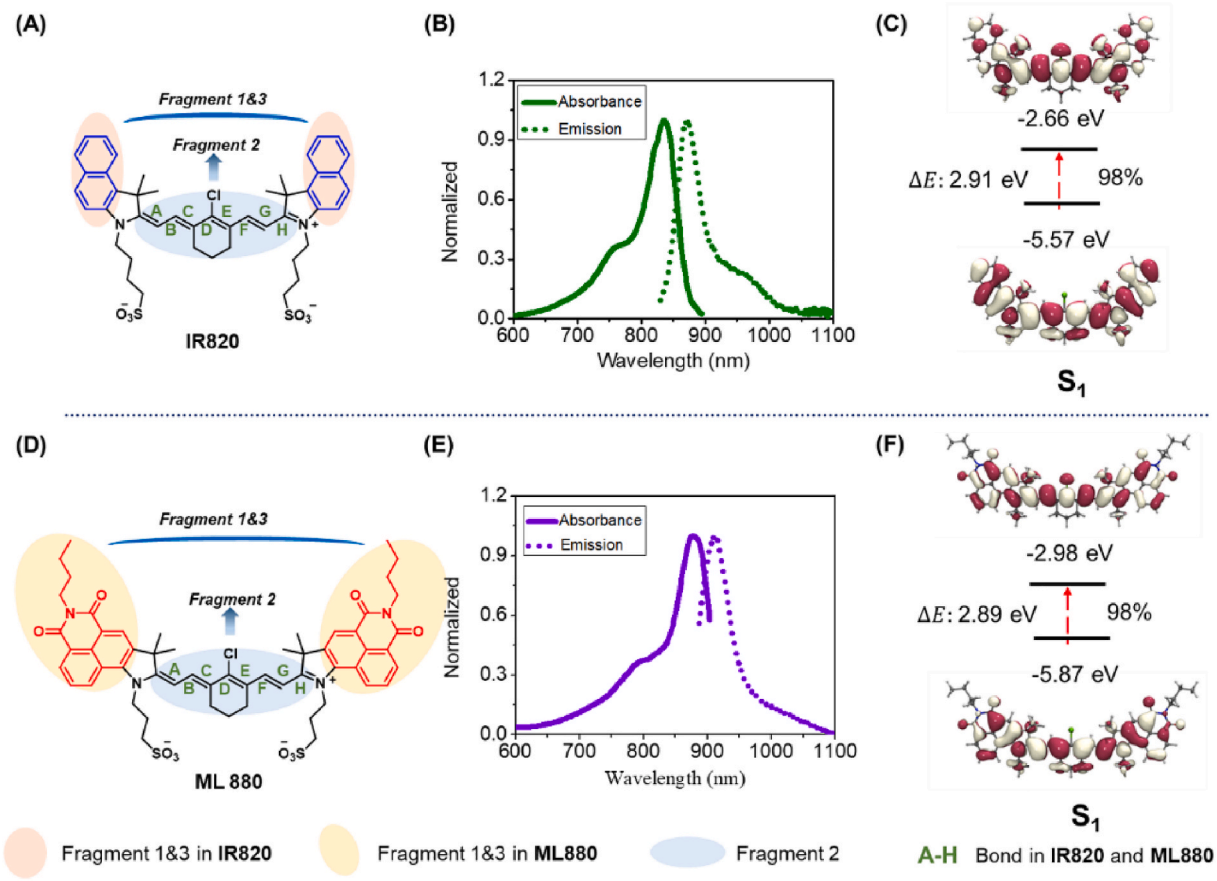

Fig. 1. The structure and normalized absorbance and emission spectrum of **IR820** (A, B) and **ML880** (D,E) in DMSO. The HOMO and LUMO distributions (isovalue = 0.01 a.u.) of **IR820** (C) and **ML880** (F) based on the optimized S1 geometries.

Interestingly, for HOMOs, both **ML880** and **IR820** possessed 30% contribution from fragment 1&3 and 70% contribution from fragment 2. However, for LUMOs, the fragment 1&3 in **ML880** possess 25% contribution which was significantly larger than that of 12% in **IR820**, indicating the introduced naphthalimide group played a key role in enhancing the electron delocalization effect. To further quantitatively study the extent of delocalization, the ODI (Orbital delocalization index) coefficient was calculated as shown in Table S3. The smaller the ODI is, the more delocalized the orbitals are. The ODI coefficients of HOMO/LUMO (4.17/4.97) of **ML880** were smaller than those of **IR820** (4.38/6.08), showing **ML880** was more delocalized than **IR820**. In short, covalent combination between naphthalimide and cyanine can lead to stronger delocalization of electronic structure and larger redshift in emission.

3.2. Photochemical properties of ML880

Since the fluorescence intensity of **ML880** in PBS was very weak, we speculated that **ML880** had good photodynamic or photothermal effect. Next, the photothermal and photodynamic properties of **ML880** were investigated upon 880 nm laser irradiation. Under different concentrations and laser power densities, **ML880** displayed remarkable photothermal property. A temperature increase from 36.3 °C to 52.9 °C was recorded with 20 μM aqueous solution of **ML880** under 1 W cm^{-2} for 8 min (Fig. 2A and B), while only 3.5 °C increase was observed in the PBS. ROS generation was verified by commercial probe **DPBF** in vitro (Fig. S4) and **DCFH-DA** in HepG2 cells [36]. As shown in Fig. S4, the absorbance at 410 nm decreases continuously along with the irradiation under 880 nm laser, indicating that **ML880** produces singlet oxygen under 880 laser irradiation. The ESR diagram also showed the generation of singlet oxygen when **ML880** was treated with laser irradiation. The measured singlet oxygen yield of **ML880** is 0.006 (calculated using ICG as reference, of which the singlet oxygen yield in Methol is 0.008) [37]. As shown in Fig. 2C and D, the fluorescence intensity of **DCFH-DA** was 2.3-fold higher than the control group without laser irradiation, demonstrating that **ML880** could produce ROS under 880 nm laser irradiation. Moreover, there was no dark cytotoxicity observed even when high concentration of **ML880** was used (100 μM), suggesting the dye had good biocompatibility (Fig. S3). In contrast, the cell viability decreased when increasing the concentration of **ML880** upon irradiation with a 0.5 W cm^{-2} laser for 5 min, demonstrating that the photothermal and photodynamic effect of the dye in cells could be triggered by NIR irradiation.

3.3. Characteristic analysis of nanohybrids

ROS-responsive mesoporous organosilica nanocarrier (**RMON**) was designed to co-load **ML880** and **NBDHEX** [38–40] with PCM as the thermal responsive gatekeeper [41], thus constructing nanomedicine **NBD&ML@RMON**. The nanocarrier could be degraded by the high level of H_2O_2 in the tumor cells, and the ROS produced by **ML880** also accelerated the degradation of **RMON**, exerting the photo controlled release behavior at the tumor site [42–44].

RMON was prepared using H_2O_2-responsive thioacetal fragment organosilane and tetraethoxysilane (Scheme S2). The morphology of **RMON** was observed by TEM and SEM, which exhibited spherical particles with an average diameter of 91 ± 5.6 nm (Fig. S5). The pore size distribution of **RMON** showed a peak centered at 2.56 nm, the BET surface area was 972.4 m^2/g and the pore volume was 0.62 cm^3/g, which was suitable as a drug delivery nanocarrier (Fig. S6). The

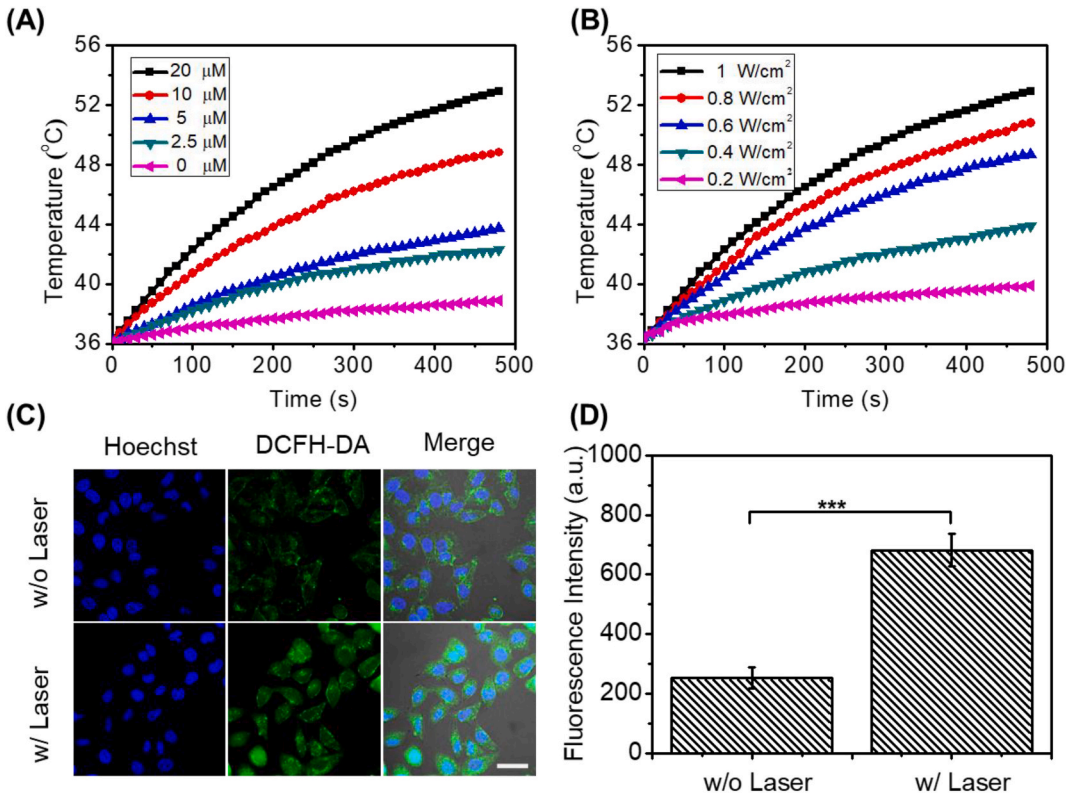

Fig. 2. PTT and PDT effects of small molecular dye **ML880**. Temperature curves of **ML880** in PBS solutions at different concentrations (A) and different laser power densities (B). (C) Fluorescence images and (D) ROS levels of **DCFH-DA** stained HepG2 cells with different treatments. Scale bar: 25 μm ***P < 0.001.

degradability of **RMON** could be confirmed by dynamic light scattering (DLS; Fig. 3A) and TEM (Fig. S7). As was shown, the degradation fragment size of **RMON** co-incubated with H_2O_2 is around 5.6 nm, which could be eliminated from the body through renal clearance [45,46]. After being co-loaded with **ML880** and NBDHEX and modified with PCM, nanomedicine **NBD&ML@RMON** was constructed with an

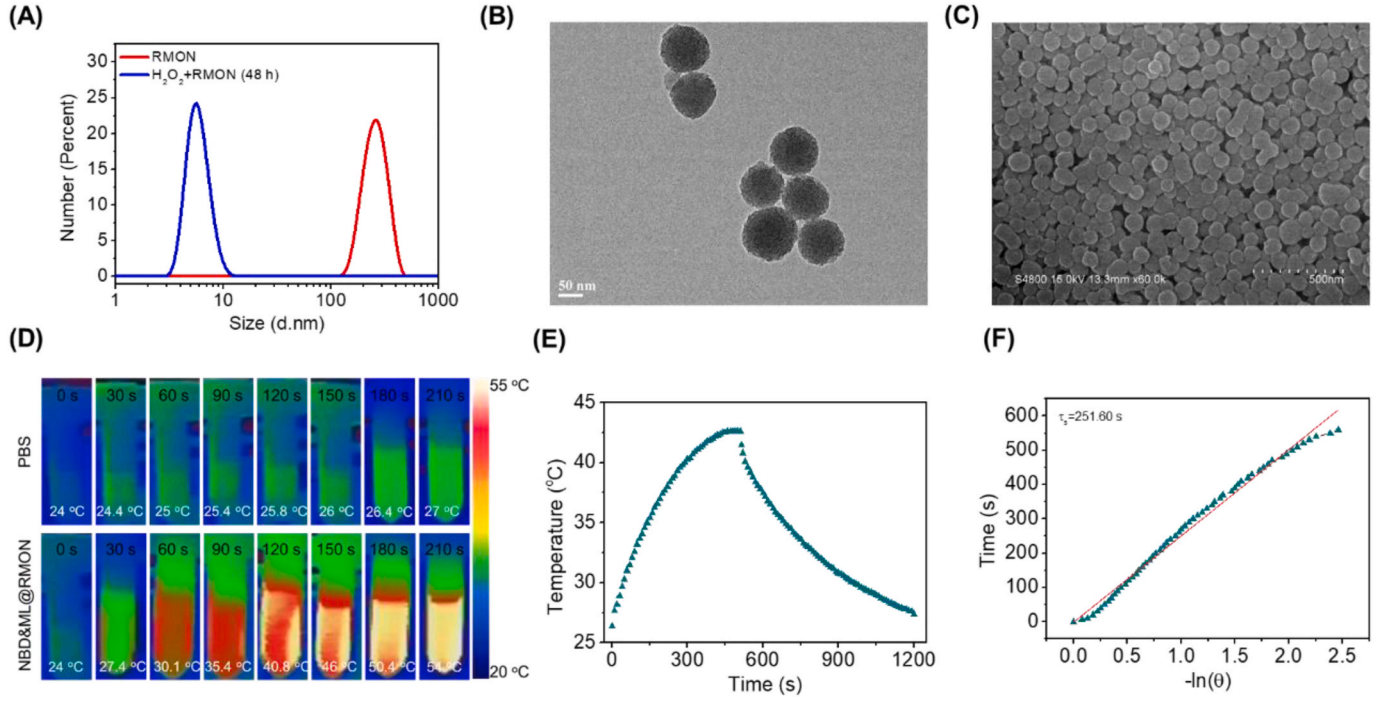

Fig. 3. Property assessment of nanohybrid **NBD&ML@RMON**. (A) DLS of **RMON** and **RMON** co-incubated with H_2O_2 (100 μM) for 48 h. (B) TEM and (C) SEM image of **NBD&ML@RMON**. (D) Photothermal images of **NBD&ML@RMON** (1 mg/mL) under 880 nm laser irradiation (1 W cm^{-2}). (E) Temperatures of the solutions of **NBD&ML@RMON** upon irradiating with an 880 nm laser (1 W cm^{-2}) for 500 s and then stopping the irradiation. (F) Graph of the cooling period of the time versus the negative natural logarithm of the temperature.

average diameter of 96 ± 4.1 nm (Fig. 3B and C). The size of nanoparticles was slightly increased without any morphology change of nanoparticles. Furthermore, the surface of the nanocarrier is negatively charged (Fig. S8), which will help to prolong blood circulation and reduce systemic toxicity. The loading rate of NBDHEX and **ML880** were calculated to be 5% and 3.5%, respectively, according to the standard curves of NBDHEX and ML880 (Fig. S9).

3.4. Photochemical properties of NBD&ML@RMON

Firstly, the photothermic property of **NBD&ML@RMON** was probed in the PBS solution. Upon NIR laser irradiation (880 nm, 1 W cm^{-2}, 210 s), photothermal images were recorded longitudinally. The **NBD&ML@RMON** dispersion dramatically increased the solution temperature. The temperature increase of **NBD&ML@RMON** ($\Delta T = 30$ °C) NPs was much higher than that of PBS ($\Delta T = 3$ °C) (Fig. 3D). The significant temperature increase clearly demonstrated the ultra efficient photothermal property of **NBD&ML@RMON**. Then the photothermal conversion efficiencies (η, PTCE) were also measured by following a reported method [47]. A steady-state temperature was recorded through the heating and cooling process and the PTCE was calculated to be 65.4% (Fig. 3E and F). As shown in Fig. S10, **NBD&ML@RMON** exhibited outstanding thermal stability and photostability, showing no degradation after four cycles of heating and cooling under continuous 880 nm laser irradiation. Meanwhile, the photodynamic property of **NBD&ML@RMON** was also evaluated inHepG2 cells. The fluorescence intensity of **DCFH-DA** was 3-fold higher than the control group without laser irradiation, demonstrating that **NBD&ML@RMON** could produce ROS under 880 nm laser irradiation (Fig. S11).

Then the property of NIR light-controlled release of **NBD&ML@RMON** was investigated under intermittent 880 nm laser irradiation. In Fig. S12, after being placedin a constant temperature water bath (37 °C) after 30 min, **NBD&ML@RMON** release amount was only 24.3% without laser irradiation. In contrast, in the case of 880 nm laser intermittent irradiation, the total amount release of NBDHEX was gradually increased. At the time point of 17 min, the cumulative release rate of NBDHEX was 66.5%. In the absence of light, the cumulative release of NBDHEX was negligible. The incubation time prolonged to 3 h was also tested (Fig. S12b). The drug release gradually stabilized after incubation for 2 h. The cumulative drug release of NBDHEX in 3 h was 26.1%. Meanwhile the cumulative drug release of **NBD&ML@RMON** under 42 °C water bath was 78.2%. These results indicated that approximately 52% of the NBDHEX was released through thermal response. Moreover, drug release curve of **NBD&ML@RMON** under different H_2O_2 concentrations was also recorded (Fig. S12b). The cumulative drug release of **NBD&ML@RMON** after 3 h was 27.4%, 39.1% and 51.7% when H_2O_2 concentration was 1 μM, 100 μM and 1 mM, respectively. Cellular uptake of **NBD&ML@RMON** was assessed through confocal microscopy. The fluorescence intensity of cells cultured for 24h was 1.8-folder higher than that of cells cultured for 12h, which indicated the cell uptake of the **NBD&ML@RMON** (Fig. S13). Photo-controlled release of the drug was also examined in HepG2 cells. The fluorescence intensity of NBDHEX with laser irradiation was 1.5-fold brighter than the control group without laser. The PCM was melted by the photothermal effect produced by **ML880**, which caused the drug NBDHEX to be released from **NBD&ML@RMON** into the cells, revealing that NIR laser irradiation accelerated the release of the drug from nanohybrid (Fig. S14). The above data fully confirmed the good ability of the NIR light-controlled release drug of nanohybrid **NBD&ML@RMON**.

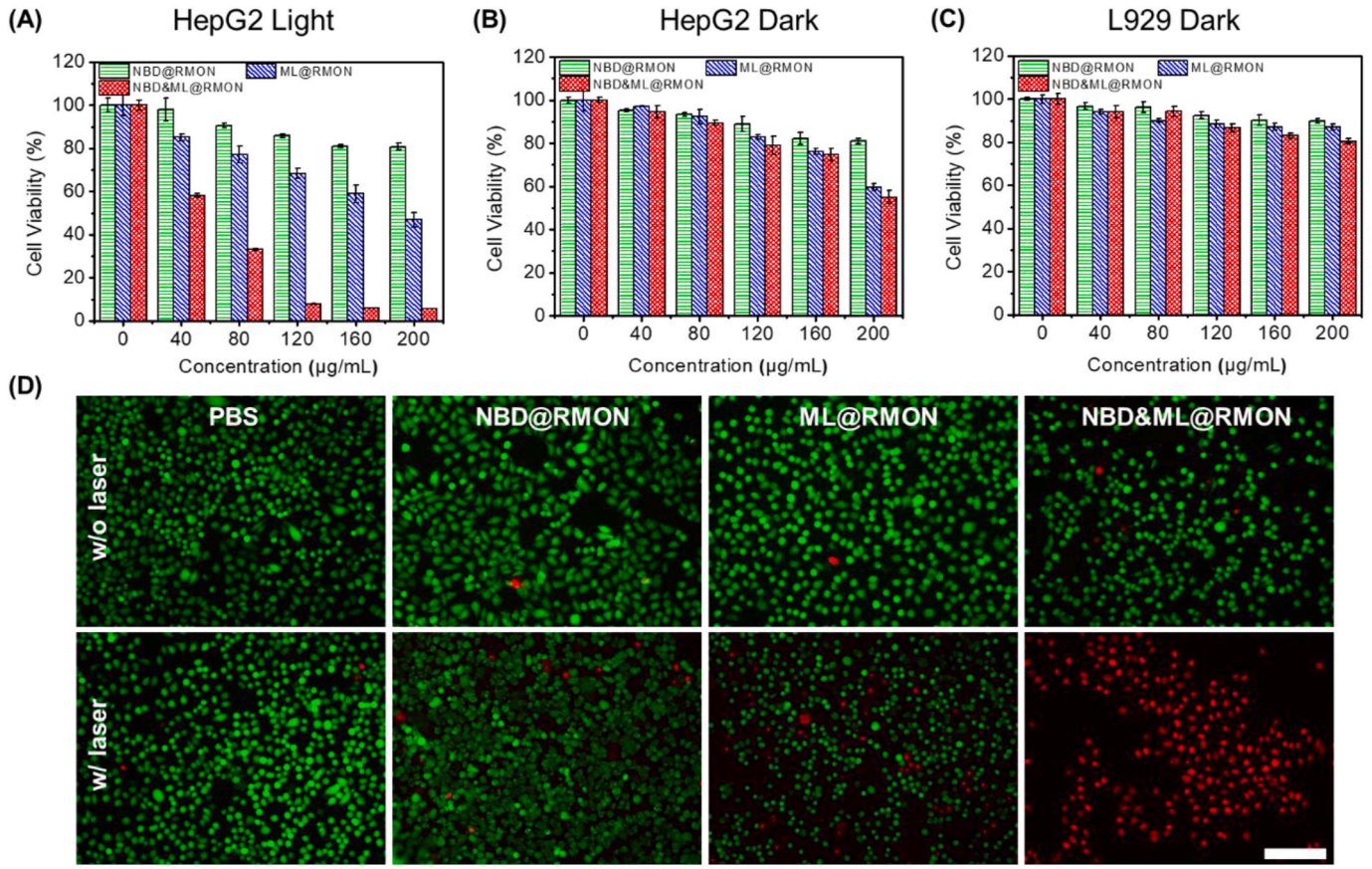

Fig. 4. Cell viability of HepG2 cells incubated with **NBD@RMON**, **ML@RMON** and **NBD&ML@RMON** at various concentrations (A) after NIR light irradiation (880 nm, 1 W cm^{-2}, 5 min) and (B) in the dark. (C) Dark cytotoxicity of L929 cells incubated with NPs. (D) CLSM images of HepG2 cells subjected to different treatments according to the live and dead cell assays (green fluorescence, calcein AM staining living cells; and red fluorescence, PI staining dead cells; scale bar = 100 μm).

3.5. Cytotoxicity of nanohybrids in cells

The phototoxicity of NPs to HepG2, L929 and Lo2 cells was examined via MTT assay. As shown in Fig. 4A, dose-dependent cytotoxicity of **NBD&ML@RMON** against the HepG2 was observed after the cells were irradiated by 880 nm laser, while neither **NBD@RMON** nor **ML@RMON** exhibited significant cytotoxicity. Nearly no cytotoxicity was observed after the HepG2 cells were treated with 160 μg/mL nanohybrids in the dark (Fig. 4B). The cytotoxicity of nanohybrids towards normal cells was also investigated. All of the nanohybrids showed negligible cytotoxicity in L929 cells (Fig. 4C) and Lo2 cells(Fig. S15), suggesting that **NBD&ML@RMON** had good biocompatibility. In the flow cytometry-based apoptotic cells analysis of HepG2 cells, the apoptosis rate detected using Annexin V-FITC/Propidium Iodide (PI) staining is less than 1% after treated with PBS, **NBD@RMON**, whether under irradiation or not. After treatment with **ML@RMON**, 11.9% of cell apoptosis is recorded under irradiation while only 0.6% in the absence of laser. After being treated with **NBD&ML@RMON**, 92.6% and 0.6% of cell apoptosis was recorded with and without irradiation respectively, which is consistent with the results of cytotoxicity experiments (Fig. S16).These results demonstrated that the over-express H_2O_2 in tumor cells and the increased temperature and ROS produced by **ML880** upon NIR laser were efficient enough to destroy the nanocarrier. Then the co-loaded chemotherapy drug NBDHEX could be control-released, realizing combining PTT/PDT/chemotherapies to kill cancer cells. To easily visualize the effectiveness of phototherapeutic performance of **NBD&ML@RMON**, live-dead cell staining assay was performed and the trend of cell mortality was consistent with that of MTT assay (Fig. 4D). Green fluorescence represents the live cells and red indicates the dead ones. As expected, the **NBD&ML@RMON** induced complete destruction of HepG2 cells after 880 nm laser irradiation (1 W cm^{-2}, 3 min) while nearly no killability under no laser. For the **ML@RMON** group, the light cytotoxicity was also higher than the dark condition. However, strong green fluorescence was observed in the PBS and **NBD@RMON** groups with or without light, indicating that strong cytotoxicity was aroused by coexistence of the **NBD&ML@RMON** and laser irradiation (Fig. 4D).

3.6. In vivo tumor inhibition

Photothermal images were recorded longitudinally after intravenous injection of NBDHEX or **NBD&ML@RMON** into HepG2 tumor-bearing mice to obtain the optimal time point for therapy [48–50]. Upon 880 nm laser irradiation, no obvious temperature changes in the tumor site were observed in the group treated with NBDHEX. After tail vein injection with **NBD&ML@RMON**, the highest temperature could reach 45.7 °C at 18 h post injection while fall to 43.6 °C at 24 h post injection, which means the maximum accumulation of **NBD&ML@RMON** in the tumor region was around 18 h post injection. These results also showed the prominent enhanced permeability and retention effect (EPR) and the photothermal effect of the nanohybrid (Fig. 5A). Then the mice were sacrificed and harvested the main organs and tumors to analyze the tissue distribution of NBDHEX. The experiments revealed that the highest concentration of NBDHEX (6.51 ng/mg) was detected in the tumor region of the mice treated with **NBD&ML@RMON** (Fig. 5B), while only 1.74 ng/mg of NBDHEX was detected in the group treated with free NBDHEX, indicating high tumor accumulation of **NBD&ML@RMON**.

Antitumor potency of the nanohybrids was investigated using HepG2 tumor-bearing Balb/c female nude mice (Fig. 6A). Mice were divided into seven groups randomly, as follows: Group 1: Saline; Group 2: Free NBDHEX; Group 3: **NBD@RMON**; Group 4: **ML@RMON**; Group 5: **ML@RMON** + laser; Group 6: **NBD&ML@RMON**; Group 7: **NBD&ML@RMON** + laser. As shown in Fig. 6B, the tumor growth in group 5 was evidently suppressed, suggesting that the PTT and PDT induced by **ML880** under NIR laser irradiation could inhibit cancer effectively. Significantly, a better tumor eradication compared with other groups was observed in group 7, indicating that cooperative interactions between PTT/PDT/chemotherapy could potentially increase the antitumor efficacy. The weights of all the mice in seven groups slowly increased, indicating that the treatments did not cause systemic toxic effects on mice (Fig. 6C). After 15-day therapy, mice were then sacrificed and harvested the main organs and tumors. The anatomized tumor displayed eradication and the lowest values in size and weight in group 7 than those in the oth-er six groups (Fig. 6D and E). It was worth noting that the tumor growth inhibition rate of Group 5 and Group 7 reached 84.3%, and 94.3%, respectively (Fig. 6F). The phototherapeutic effect produced by **ML880** in Group 5 was effective to inhibit the tumor growth, while combination with chemotherapy in Group 7 produced a remarkable tumor suppression even eradication. The bioactivity of residual tumor tissues was further verified through a pathological examination by hematoxylin and eosin (H&E) staining and TUNEL experiments. The H&E staining and TUNEL of tumor slices indicated that Group 5 and 7 exerts plenty of tumor cells apoptosis (Fig. 6G and H). No obvious histopathological abnormality was observed from normal organs among seven groups, verifying the excellent biocompatibility of nanohybrids (Fig. S17). The pharmacokinetic profiles of the free NBDHEX and **NBD&ML@RMON** were further studied in Sprague-Dawley (SD) rats by determining the fluorescence intensity of NBDHEX in plasma. As shown in Fig. S18, The incorporation of NBDHEX in nanohybrids enables higher NBDHEX concentrations in the blood circulation than free NBDHEX over 48 h. The maximum plasma concentration of NBDHEX in mice injected with **NBD&ML@RMON** was 7.38 μg/mL, much higher than that of free NBDHEX, at 4.96 μg/mL. There was a significant 5.6-fold improvement in the AUC (Area Under Curve) between the **NBD&ML@RMON** (139.42 mg/L h) and free NBDHEX (24.65 mg/L h), indicating that **NBD&ML@RMON** could

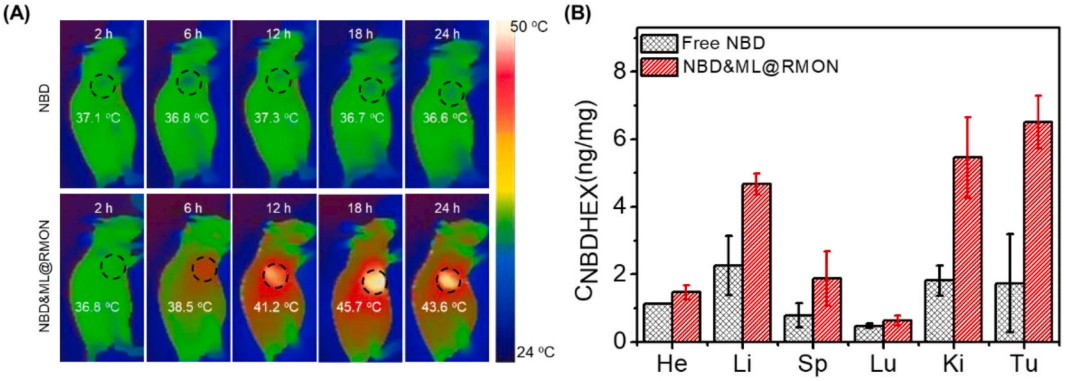

Fig. 5. (A) Photothermal imaging of the tumor region under 880 nm laser irradiation (1 W cm^{-2}, 5 min). (B) In vivo drug distribution in mice after 24h with free NBDHEX and **NBD&ML@RMON**.

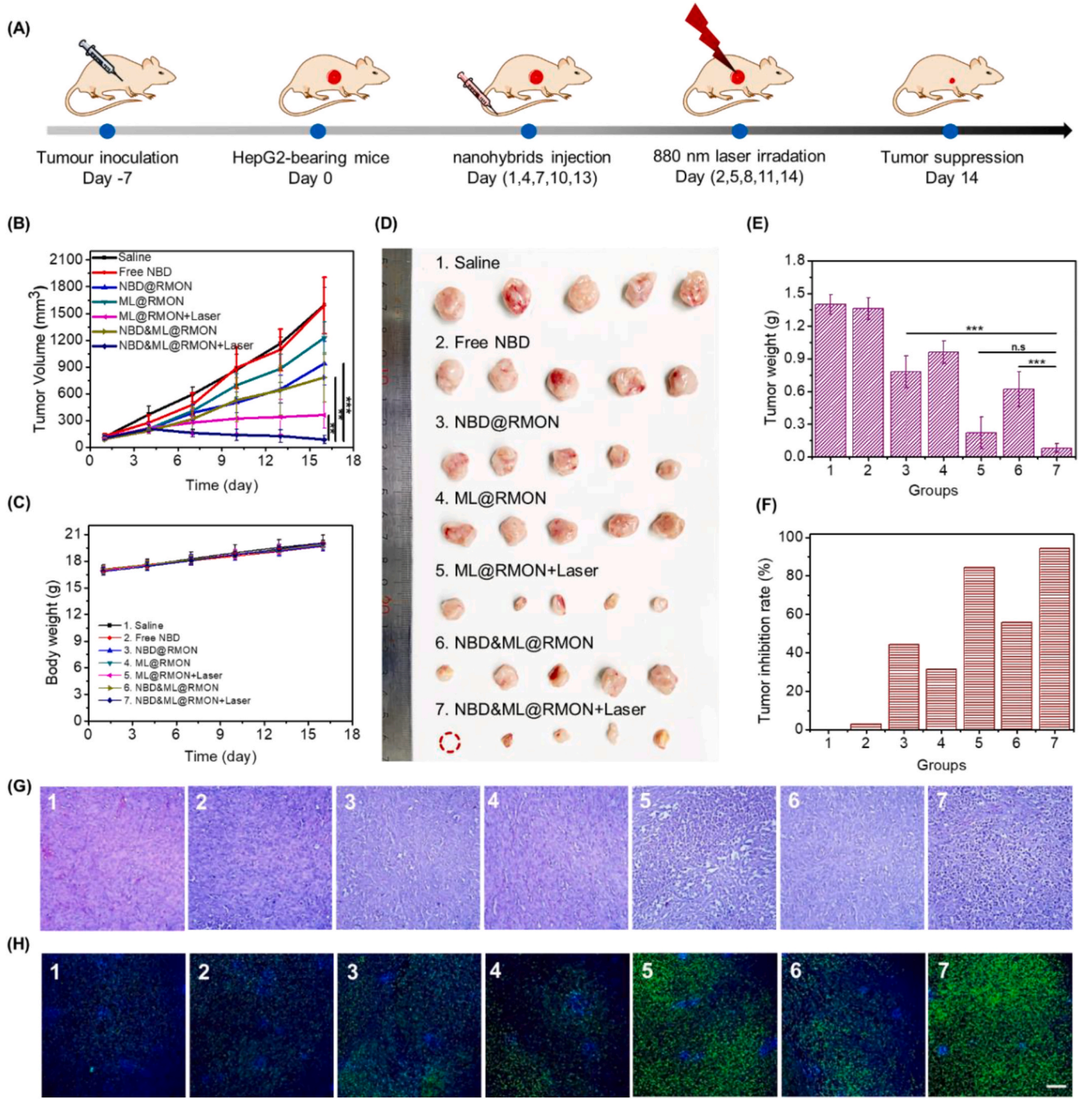

Fig. 6. In vivo assessment of NBD&ML@RMON. (A) Scheme of the timeline of experimental design. (B) Tumor volume growth curves of HepG2 tumor-bearing mice treated with various NPs. (C) Body weight changes of mice during different treatments. (D) Photos and (E) tumor weight of the dissected tumors obtained after 15-day therapy. (F) Tumor growth inhibition ratio after various treatments. (G) H&E staining and (H) CLSM images of TUNEL assay of the dissected tumor after 15-day therapy. Scale bar: 100 μm ***P < 0.001.

improve the bioavailability of NBDHEX after systematic administration.

Furthermore, immunofluorescence staining images showed that NBDHEX could inhibit GSTP1-1 effectively (Fig. S19). We further monitored the expression of apoptosis-associated proteins [51]. The mitochondrial apoptotic pathway (a major signalling way to involve in tumor cells apoptosis) associated proteins of caspase-3, Bax (pro-apoptotic protein), and Bcl-2 (antiapoptotic protein) in tumor cells were detected by Western blot, and the apoptosis-related proteins levels were shown in Fig. 7. It was found that the Bcl-2 level of Group 5/7 was obviously down-regulated, while the pro-apoptotic protein Bax was significantly up-regulated compared to other groups. Moreover, the downstream protein active-caspase 3 was highly expressed in group 5/7, which could be ascribed to massive cell apoptosis. These results showed that the HepG2 cells in Group 5 and 7 treated with **ML@RMON** and **NBD&ML@RMON** respectively were apoptosis by mitochondrial apoptosis pathway under NIR laser (880 nm) light.

4. Conclusion

In summary, a new NIR dye **ML880** with naphthimide modified

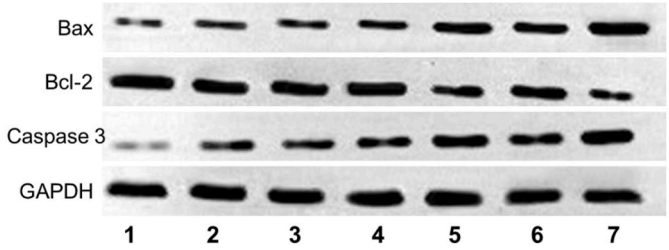

Fig. 7. Western blotting analysis of mitochondrial apoptotic pathway associated proteins in tumor tissues after therapy.

cyanine skeleton was designed and synthesized using an integration strategy. By introducing the naphthalimide moiety, **ML880** exhibited stronger electron delocalization and larger redshift in emission compared with **IR820**. Then **ML880** was encapsulated with the chemotherapy drug into photothermal/ROS dual-responsive **RMON** to construct nanomedicine **NBD&ML@RMON**. Both in vitro and in vivo experiments demonstrated excellent therapeutic effects of **NBD&ML@RMON**, implying that combined PDT/PTT/chemotherapy could remarkably inhibit tumor growth with high biosafety under 880 nm laser irradiation. Our study is a successful attempt to prolong the wavelength of traditional dyes by integration strategy and open a new platform for the future design of phototherapeutic agents by combination with various therapies in comprehensive cancer treatment.

Declaration of interests

The authors declare that they have no known competing financial interests or personal relationships that could have appeared to influence the work reported in this paper.

CRediT authorship contribution statement

Tongxia Jin: Conceptualization, Methodology, Data curation, Formal analysis, Investigation, Writing – original draft. **Di Cheng:** Conceptualization, Methodology, Data curation, Formal analysis, Investigation, Writing – original draft. **Guanyu Jiang:** Methodology, Data curation, Formal analysis, Investigation, Writing – original draft. **Wenqian Xing:** Investigation. **Peiwen Liu:** Investigation. **Bin Wang:** Investigation. **Weiping Zhu:** Conceptualization, Methodology, Data curation, Formal analysis, Resources, Writing – review & editing, Supervision, Project administration, Funding acquisition. **Haitao Sun:** Methodology, Data curation, Formal analysis, Writing – review & editing, Funding acquisition. **Zhenrong Sun:** Supervision. **Yufang Xu:** Supervision. **Xuhong Qian:** Resources, Supervision, Project administration, Funding acquisition.

Acknowledgement

This work was supported by National Natural Science Foundation of China (Grants 21878088, 12034008, 21476077, 11727810), Key projects of Shanghai Science and Technology Commission (18DZ1112703), and Shanghai Frontiers Science Center of Optogenetic Techniques for Cell Metabolism (Shanghai Municipal Education Commission, grant 2021 Sci & Tech 03-28)

Appendix A. Supplementary data

Supplementary data to this article can be found online at https://doi.org/10.1016/j.bioactmat.2021.12.009.

References

[1] G. Hong, A.L. Antaris, H. Dai, Near-infrared fluorophores for biomedical imaging, Nat. Biomed. Eng. 1 (1) (2017), https://doi.org/10.1038/s41551-016-0010.
[2] Z. Hu, C. Fang, B. Li, Z. Zhang, C. Cao, M. Cai, S. Su, X. Sun, X. Shi, C. Li, T. Zhou, Y. Zhang, C. Chi, P. He, X. Xia, Y. Chen, S.S. Gambhir, Z. Cheng, J. Tian, First-in-human liver-tumour surgery guided by multispectral fluorescence imaging in the visible and near-infrared-I/II windows, Nat. Biomed. Eng. 4 (3) (2020) 259–271, https://doi.org/10.1038/s41551-019-0494-0.
[3] J. Weber, P.C. Beard, S.E. Bohndiek, Contrast agents for molecular photoacoustic imaging, Nat. Methods 13 (8) (2016) 639–650, https://doi.org/10.1038/nmeth.3929.
[4] A.E. O'Connor, W.M. Gallagher, A.T. Byrne, Porphyrin and nonporphyrin photosensitizers in oncology: preclinical and clinical advances in photodynamic therapy, Photochem. Photobiol. 85 (5) (2009) 1053–1074, https://doi.org/10.1111/j.1751-1097.2009.00585.x.
[5] H.S. Jung, P. Verwilst, A. Sharma, J. Shin, J.L. Sessler, J.S. Kim, Organic molecule-based photothermal agents: an expanding photothermal therapy universe, Chem. Soc. Rev. 47 (7) (2018) 2280–2297, https://doi.org/10.1039/C7CS00522A.
[6] M.R. Detty, S.L. Gibson, S.J. Wagner, Current clinical and preclinical photosensitizers for use in photodynamic therapy, J. Med. Chem. 47 (16) (2004) 3897–3915, https://doi.org/10.1021/jm040074b.
[7] C. Fisher, Z. Ali, J. Detsky, A. Sahgal, E. David, M. Kunz, M. Akens, E. Chow, C. Whyne, S. Burch, B.C. Wilson, A. Yee, Photodynamic therapy for the treatment of vertebral metastases: a phase I clinical trial, Clin. Cancer Res. 25 (19) (2019) 5766–5776, https://doi.org/10.1158/1078-0432.CCR-19-0673.
[8] A.T. Byrne, A.E. O'Connor, M. Hall, J. Murtagh, K. O'Neill, K.M. Curran, K. Mongrain, J.A. Rousseau, R. Lecomte, S. McGee, J.J. Callanan, D.F. O'Shea, W. M. Gallagher, Vascular-targeted photodynamic therapy with BF2-chelated Tetraaryl-Azadipyrromethene agents: a multi-modality molecular imaging approach to therapeutic assessment, Br. J. Cancer 101 (9) (2009) 1565–1573, https://doi.org/10.1038/sj.bjc.6605247.
[9] W.R. Chen, R.L. Adams, R. Carubelli, R.E. Nordquist, Laser-photosensitizer assisted immunotherapy: a novel modality for cancer treatment, Cancer Lett. 115 (1) (1997) 25–30, https://doi.org/10.1016/S0304-3835(97)04707-1.
[10] X.S. Li, G.L. Ferrel, M.C. Guerra, T. Hode, J.A. Lunn, O. Adalsteinsson, R. E. Nordquist, H. Liu, W.R. Chen, Preliminary safety and efficacy results of laser immunotherapy for the treatment of metastatic breast cancer patients, Photochem. Photobiol. Sci. 10 (5) (2011) 817–821, https://doi.org/10.1039/C0PP00306A.
[11] S.B. Qiu, D.D. Dai, C.L. Guo, Z.L. Sun, H. Li, X.H. Qian, Y.J. Yang, Amino-substituted C-coumarins: synthesis, spectral characterizations and their applications in cell imaging, Dyes Pigments 163 (2019) 55–61, https://doi.org/10.1016/j.dyepig.2018.11.012.
[12] X. Luo, J. Li, J. Zhao, L. Gu, X. Qian, Y. Yang, A general approach to the design of high-performance near-infrared (NIR) D-π-A type fluorescent dyes, Chin. Chem. Lett. 30 (4) (2019) 839–846, https://doi.org/10.1016/j.cclet.2019.03.012.
[13] Z. Lei, X. Li, X. Luo, H. He, J. Zheng, X. Qian, Y. Yang, Bright, stable, and biocompatible organic fluorophores absorbing/emitting in the deep near-infrared spectral region, Angew Chem. Int. Ed. Engl. 56 (11) (2017) 2979–2983, https://doi.org/10.1002/ange.201612301.
[14] M. Fu, Y. Xiao, X. Qian, D. Zhao, Y. Xu, A design concept of long-wavelength fluorescent analogs of rhodamine dyes: replacement of oxygen with silicon atom, Chem Commun (Camb) 15 (2008) 1780–1782, https://doi.org/10.1039/B718544H.
[15] J.-A. Richard, M. Massonneau, P.-Y. Renard, A. Romieu, 7-Hydroxycoumarin−Hemicyanine hybrids: a new class of far-red emitting fluorogenic dyes, Org. Lett. 10 (19) (2008) 4175–4178, https://doi.org/10.1021/ol801582w.
[16] L. Yuan, W. Lin, Y. Yang, H. Chen, A unique class of near-infrared functional fluorescent dyes with carboxylic-acid-modulated fluorescence ON/OFF switching: rational design, synthesis, optical properties, theoretical calculations, and applications for fluorescence imaging in living animals, J. Am. Chem. Soc. 134 (2) (2012) 1200–1211, https://doi.org/10.1021/ja209292b.
[17] E.D. Cosco, J.R. Caram, O.T. Bruns, D. Franke, R.A. Day, E.P. Farr, M.G. Bawendi, E.M. Sletten, Flavylium polymethine fluorophores for near- and shortwave infrared imaging, Angew Chem. Int. Ed. Engl. 56 (42) (2017) 13126–13129, https://doi.org/10.1002/anie.201706974.
[18] Z. Lei, C. Sun, P. Pei, S. Wang, D. Li, X. Zhang, F. Zhang, Stable, wavelength-tunable fluorescent dyes in the NIR-II region for in vivo high-contrast bioimaging and multiplexed biosensing, Angew Chem. Int. Ed. Engl. 58 (24) (2019) 8166–8171, https://doi.org/10.1002/anie.201904182.
[19] X. Yao, M. Li, B. Li, C. Xue, K. Cai, Y. Zhao, Z. Luo, Tumor-targeted upconverting nanoplatform constructed by host-guest interaction for near-infrared-light-actuated synergistic photodynamic-/chemotherapy, Chem. Eng. J. 390 (2020), https://doi.org/10.1016/j.cej.2020.124516.
[20] X. Wang, M. Li, Y. Hou, Y. Li, X. Yao, C. Xue, Y. Fei, Y. Xiang, K. Cai, Y. Zhao, Z. Luo, Tumor-microenvironment-activated in situ self-assembly of sequentially responsive biopolymer for targeted photodynamic therapy, Adv. Funct. Mater. 30 (40) (2020), https://doi.org/10.1002/adfm.202000229.
[21] X. Li, J.F. Lovell, J. Yoon, X. Chen, Clinical development and potential of photothermal and photodynamic therapies for cancer, Nat. Rev. Clin. Oncol. 17 (11) (2020) 657–674, https://doi.org/10.1038/s41571-020-0410-2.
[22] T. Jin, C. Huang, M. Cui, Y. Yang, Z. Wang, W. Zhu, X. Qian, Supramolecular ensembles modified by near-infrared dyes and their biological applications, J. Mater. Chem. B 8 (47) (2020) 10686–10699, https://doi.org/10.1039/D0TB01829E.

[23] Y. Liu, P. Bhattarai, Z. Dai, X. Chen, Photothermal therapy and photoacoustic imaging via nanotheranostics in fighting cancer, Chem. Soc. Rev. 48 (7) (2019) 2053–2108, https://doi.org/10.1039/C8CS00618K.
[24] H.-h. Sha, Z. Wang, S.-c. Dong, T.-m. Hu, S.-w. Liu, J.-y. Zhang, Y. Wu, R. Ma, J.-z. Wu, D. Chen, J.-f. Feng, 6-(7-nitro-2,1,3-benzoxadiazol-4-ylthio) hexanol: a promising new anticancer compound, Biosci. Rep. 38 (1) (2018), https://doi.org/10.1042/BSR20171440.
[25] T. Lim, J.Y. Ryoo, M. Jang, M.S. Han, Ligand-free Suzuki-Miyaura cross-coupling with low Pd content: rapid development by a fluorescence-based high-throughput screening method, Org. Biomol. Chem. 19 (5) (2021) 1009–1016, https://doi.org/10.1039/D0OB02359K.
[26] Q. Jin, Y. Hu, J. Shen, B. Li, C. Kan, A novel 1,8-naphthalimide green fluorescent dye and its corresponding intrinsically fluorescent polyurethane latexes, J. Coating Technol. Res. 14 (3) (2017) 571–582, https://doi.org/10.1007/s11998-016-9874-5.
[27] S.A. Choi, C.S. Park, O.S. Kwon, H.K. Giong, J.S. Lee, T.H. Ha, C.S. Lee, Structural effects of naphthalimide-based fluorescent sensor for hydrogen sulfide and imaging in live zebrafish, Sci. Rep. 6 (2016) 26203, https://doi.org/10.1038/srep26203.
[28] J. Zhengneng, L. Najun, W. Chuanfeng, J. Huajiang, L. Jianmei, Z. Qizhong, Synthesis and fluorescence property of some novel 1,8-naphthalimide derivatives containing a thiophene ring at the C-4 position, Dyes Pigments 96 (1) (2013) 204–210, https://doi.org/10.1016/j.dyepig.2012.07.018.
[29] T. Zimmermann, L. Hennig, Ring transformations of heterocyclic compounds. XXII [1]. Pyrido[1,2-a]indolium salts from 2-methyl-3H-indoles by pyrylium mediated three carbon annelation, J. Heterocycl. Chem. 39 (2002) 255.
[30] A. Grichine, A. Haefele, S. Pascal, A. Duperray, R. Michel, C. Andraud, O. Maury, Millisecond lifetime imaging with a europium complex using a commercial confocal microscope under one or two-photon excitation, Chem. Sci. 5 (9) (2014) 3475–3485, https://doi.org/10.1039/C4SC00473F.
[31] D.E. Lynch, A.N. Kirkham, M.Z.H. Chowdhury, E.S. Wane, J. Heptinstall, Water soluble squaraine dyes for use as colorimetric stains in gel electrophoresis, Dyes Pigments 94 (3) (2012) 393–402, https://doi.org/10.1016/j.dyepig.2012.02.001.
[32] J. Liu, W. Tang, L. Sheng, Z. Du, T. Zhang, X. Su, S.X. Zhang, Effects of substituents on metastable-state photoacids: design, synthesis, and evaluation of their photochemical properties, Chem. Asian J. 14 (3) (2019) 438–445, https://doi.org/10.1002/asia.201801687.
[33] P. Choi, K. Noguchi, M. Ishiyama, W.A. Denny, J. Jose, A mitochondria-selective near-infrared-emitting fluorescent dye for cellular imaging studies, Bioorg. Med. Chem. Lett 28 (11) (2018) 2013–2017, https://doi.org/10.1016/j.bmcl.2018.05.001.
[34] T.M. Ebaston, F. Nakonechny, E. Talalai, G. Gellerman, L. Patsenker, Iodinated xanthene-cyanine NIR dyes as potential photosensitizers for antimicrobial photodynamic therapy, Dyes Pigments 184 (2021), https://doi.org/10.1016/j.dyepig.2020.108854.
[35] Y.D. Zhang, Q.W. Huang, C. Ma, X.Y. Liu, H.X. Zhang, Magnetic fluorescent molecularly imprinted nanoparticles for detection and separation of transferrin in human serum, Talanta 188 (2018) 540–545, https://doi.org/10.1016/j.talanta.2018.06.002.
[36] Y. Nosaka, A.Y. Nosaka, Generation and detection of reactive oxygen species in photocatalysis, Chem. Rev. 117 (17) (2017) 11302–11336, https://doi.org/10.1021/acs.chemrev.7b00161.
[37] N.S. James, Y. Chen, P. Joshi, T.Y. Ohulchanskyy, M. Ethirajan, M. Henary, L. Strekowsk, R.K. Pandey, Evaluation of polymethine dyes as potential probes for near infrared fluorescence imaging of tumors: part - 1, Theranostics 3 (9) (2013) 692–702, https://doi.org/10.7150/thno.5922.
[38] L. Maggini, I. Cabrera, A. Ruiz-Carretero, E.A. Prasetyanto, E. Robinet, L. De Cola, Breakable mesoporous silica nanoparticles for targeted drug delivery, Nanoscale 8 (13) (2016) 7240–7247, https://doi.org/10.1039/C5NR09112H.
[39] S. Hua, X. Wang, F. Chen, S. Gou, Novel conjugates with dual suppression of glutathione S-transferases and tryptophan-2,3-dioxygenase activities for improving hepatocellular carcinoma therapy, Bioorg. Chem. 92 (2019) 103191, https://doi.org/10.1016/j.bioorg.2019.103191.
[40] L. Tentori, A.S. Dorio, E. Mazzon, A. Muzi, A. Sau, S. Cuzzocrea, P. Vernole, G. Federici, A.M. Caccuri, G. Graziani, The glutathione transferase inhibitor 6-(7-nitro-2,1,3-benzoxadiazol-4-ylthio)hexanol (NBDHEX) increases temozolomide efficacy against malignant melanoma, Eur. J. Cancer 47 (8) (2011) 1219–1230, https://doi.org/10.1016/j.ejca.2010.12.008.
[41] J. Qiu, D. Huo, J. Xue, G. Zhu, H. Liu, Y. Xia, Encapsulation of a phase-change material in nanocapsules with a well-defined hole in the wall for the controlled release of drugs, Angew Chem. Int. Ed. Engl. 58 (31) (2019) 10606–10611, https://doi.org/10.1002/anie.201904549.
[42] M. Wang, Y. Zhai, H. Ye, Q. Lv, B. Sun, C. Luo, Q. Jiang, H. Zhang, Y. Xu, Y. Jing, L. Huang, J. Sun, Z. He, High Co-loading capacity and stimuli-responsive release based on cascade reaction of self-destructive polymer for improved chemo-photodynamic therapy, ACS Nano 13 (6) (2019) 7010–7023, https://doi.org/10.1021/acsnano.9b02096.
[43] Q. Pei, X. Hu, X. Zheng, S. Liu, Y. Li, X. Jing, Z. Xie, Light-activatable red blood cell membrane-camouflaged dimeric prodrug nanoparticles for synergistic photodynamic/chemotherapy, ACS Nano 12 (2) (2018) 1630–1641.
[44] J. Li, K. Wei, S. Zuo, Y. Xu, Z. Zha, W. Ke, H. Chen, Z. Ge, Light-triggered clustered vesicles with self-supplied oxygen and tissue penetrability for photodynamic therapy against hypoxic tumor, Adv. Funct. Mater. 27 (33) (2017), https://doi.org/10.1002/adfm.201702108.
[45] H.S. Choi, W. Liu, P. Misra, E. Tanaka, J.P. Zimmer, B. Itty Ipe, M.G. Bawendi, J. V. Frangioni, Renal clearance of quantum dots, Nat. Biotechnol. 25 (10) (2007) 1165–1170, https://doi.org/10.1038/nbt1340.
[46] B. Du, X. Jiang, A. Das, Q. Zhou, M. Yu, R. Jin, J. Zheng, Glomerular barrier behaves as an atomically precise bandpass filter in a sub-nanometre regime, Nat. Nanotechnol. 12 (11) (2017) 1096–1102, https://doi.org/10.1038/nnano.2017.170.
[47] D.K. Roper, W. Ahn, M. Hoepfner, Microscale heat transfer transduced by surface plasmon resonant gold nanoparticles, J. Phys. Chem. C 111 (9) (2007) 3636–3641, https://doi.org/10.1021/jp064341w.
[48] M. Qian, L. Chen, Y. Du, H. Jiang, T. Huo, Y. Yang, W. Guo, Y. Wang, R. Huang, Biodegradable mesoporous silica achieved via carbon nanodots-incorporated framework swelling for debris-mediated photothermal synergistic immunotherapy, Nano Lett. 19 (12) (2019) 8409–8417, https://doi.org/10.1021/acs.nanolett.9b02448.
[49] K. Deng, Z. Hou, X. Deng, P. Yang, C. Li, J. Lin, Enhanced antitumor efficacy by 808 nm laser-induced synergistic photothermal and photodynamic therapy based on a indocyanine-green-attached $W_{18}O_{49}$ nanostructure, Adv. Funct. Mater. 25 (47) (2015) 7280–7290, https://doi.org/10.1002/adfm.201503046.
[50] Q. Chen, J. Wen, H. Li, Y. Xu, F. Liu, S. Sun, Recent advances in different modal imaging-guided photothermal therapy, Biomaterials 106 (2016) 144–166, https://doi.org/10.1016/j.biomaterials.2016.08.022.
[51] S. Zhang, S. Nie, D. Huang, Y. Feng, M. Xie, A novel polysaccharide from Ganoderma atrum exerts antitumor activity by activating mitochondria-mediated apoptotic pathway and boosting the immune system, J. Agric. Food Chem. 62 (7) (2014) 1581–1589, https://doi.org/10.1021/jf4053012.